Second-order calculation of the local density of states above a nanostructured surface

Felix Rüting, Svend-Age Biehs,* Oliver Huth, and Martin Holthaus
Institut für Physik, Carl von Ossietzky Universität, D-26111 Oldenburg, Germany
(Received 2 February 2010; revised manuscript received 21 April 2010; published 24 September 2010)

We have numerically implemented a perturbation series for the scattered electromagnetic fields above rough surfaces, due to Greffet, allowing us to evaluate the local density of states to second order in the surface profile function. We present typical results for thermal near fields of surfaces with regular nanostructures, investigating the relative magnitude of the contributions appearing in successive orders. The method is then employed for estimating the resolution limit of an idealized near-field scanning thermal microscope.

DOI: 10.1103/PhysRevB.82.115443 PACS number(s): 44.40.+a, 78.67.−n, 05.40.−a, 41.20.Jb

I. INTRODUCTION

Quite recently there has been a notable increase in experimental activities aiming at the exploration of properties of thermally generated fluctuating electromagnetic fields close to the surface of some material, and at detecting the near-field mediated heat transfer.[1–3] Hu *et al.*[4] have measured the near-field thermal radiation between micron-spaced glass plates, and have demonstrated that the resulting near-field heat transfer exceeds the far-field limit set by Planck's blackbody radiation law. Next, Narayanaswamy *et al.* and Shen *et al.* have studied the heat transfer between microspheres and flat substrates, with emphasis on the coupling of surface phonon polaritons across the gap between them, and have reported heat-transfer coefficients three orders of magnitude above the blackbody radiation limit.[5,6] Then Rousseau *et al.*[7] have carried out precise measurements of the radiative heat transfer between sodalime glass spheres with diameters of 22 or 40 μm and borosilicate glass plates for distances ranging from 30 nm to 2.5 μm, and have verified theoretical predictions based on fluctuational electrodynamics[1,8] with impressive accuracy. On the other hand, significant progress has been made at using near-field effects for imaging. Kittel *et al.* are developing a device termed near-field scanning thermal microscope (NSThM) (Refs. 9–11) which does not yet seem capable of highly accurate quantitative measurements of the near-field heat current between its sensor and the sample, but which lends itself to nanoscale thermal imaging of structured surfaces.[12] Moreover, De Wilde *et al.* have reported the successful operation of a thermal radiation scanning tunneling microscope,[13] providing images of thermally excited surface plasmons, and giving clear evidence for spatial coherence effects in near-field thermal emission.

These remarkable developments indicate that thermal near-field physics, after having been under intense theoretical investigation for some time already,[1–3,8] is breaking through to the forefront of experimental research right now. There are several compelling reasons for this trend. Besides the prospects of obtaining novel insight into fundamental physics in dielectric matter, and of developing advanced diagnostic tools for materials science, thermal near-field effects have great potential for near-field thermophotovoltaic energy conversion.[14–18]

On the theoretical side, one of the most important quantities characterizing the fluctuating thermal near field close to a dielectric surface is its local density of states (LDOS).[19] In particular, the power P transferred between a dielectric sample at temperature T_S and a nanoparticle at temperature T_P, brought into the sample's near field at a position $\boldsymbol{a}$ such that the particle may effectively be treated within the dipole approximation, and the heat transfer proceeds almost entirely via evanescent modes, is given by (see, e.g., Refs. 20–25)

$$P = \int_0^\infty d\omega 2\omega[\Theta(\omega,T_P) - \Theta(\omega,T_S)] \times[\alpha_P''(\omega)D^E(\omega,\boldsymbol{a}) + \mu_P''(\omega)D^H(\omega,\boldsymbol{a})], \quad (1)$$

where $D^E(\omega,\boldsymbol{a})$ is the electric and $D^H(\omega,\boldsymbol{a})$ is the magnetic part of the sample's LDOS at the point $\boldsymbol{a}$ of effective interaction; $\alpha_P''(\omega)$ and $\mu_P''(\omega)$ denote the imaginary part of the particle's electric and magnetic polarizability, respectively. Finally,

$$\Theta(\omega,T) = \frac{\hbar\omega}{\exp(\hbar\omega/k_BT) - 1} \quad (2)$$

is the Bose-Einstein function; the sign in Eq. (1) is chosen such that a net energy transfer from the particle to the sample, occurring for $T_P > T_S$, gives a positive P. The use of the dipole approximation underlying Eq. (1) requires that the distance of the nanoparticle from the sample's surface remains large compared to its linear size. Those frequencies which significantly contribute to the heat transfer are limited by the higher temperature $T_{max} = \max(T_P, T_S)$. Provided the polarizabilities and the LDOS exhibit no resonances in the accessible frequency regime, requiring in particular the absence of thermally excitable surface modes, the main contribution to the integral (1) merely stems from frequencies in the vicinity of the thermal frequency $\omega_{th} \approx 2.82\ k_BT/\hbar$, so that

$$P \propto \omega_{th}[\alpha_P''(\omega_{th})D^E(\omega_{th},\boldsymbol{a}) + \mu_P''(\omega_{th})D^H(\omega_{th},\boldsymbol{a})]. \quad (3)$$

Under suitable conditions, already this simple approximation can give surprisingly good results when trying to theoretically reconstruct surface images obtained with the NSThM.[12]

The possibility to experimentally assess the LDOS above nanostructured surfaces demands refined techniques for its calculation. Assuming local thermal equilibrium, and considering positions $\boldsymbol{r}$ so close to the sample's surface that the energy density is dominated by evanescent modes and the

contribution of propagating modes can be neglected, the electric and the magnetic LDOS are related to the imaginary parts of the traces of the renormalized (or "reflected") electric and magnetic Green's dyadics $\mathbb{G}_r^E$ and $\mathbb{G}_r^H$ through the relations[19]

$$D^E(\omega,\boldsymbol{r}) = \frac{\omega}{\pi c^2}\mathrm{Im\ Tr}\ \mathbb{G}_r^E(\boldsymbol{r},\boldsymbol{r}) \tag{4}$$

and

$$D^H(\omega,\boldsymbol{r}) = \frac{\omega}{\pi c^2}\mathrm{Im\ Tr}\ \mathbb{G}_r^H(\boldsymbol{r},\boldsymbol{r}). \tag{5}$$

In the present paper we exploit this connection for computing the LDOS above a nanostructured surface to second order in the surface profile, relying on an earlier formulation of the perturbation series by Greffet.[26] The method is technically involved, and soon hits practical computational limits when proceeding to higher orders. Nonetheless, we show that second-order calculations now are feasible routinely. Our work thus extends a previous study,[27] which has given first-order results, and enables us to delineate under which conditions low-order perturbation theory is sufficient. It also complements a recent investigation by Biehs and Greffet[28] who have considered rough surfaces described as stochastic Gaussian processes. In contrast, we focus on surfaces with deliberately induced, regular nanoprofiles. We proceed as follows. In Sec. II we sketch the underlying perturbative scheme,[26] and outline a few details of its numerical implementation, deferring technicalities to the Appendix. We then present results of our computations in Sec. III, first examining the relative magnitude of first- and second-order contributions, and then outlining how to quantify the resolution power of an idealized NSThM. Some conclusions are drawn in the final Sec. IV.

II. COMPUTATION OF THE GREEN'S DYADICS

In this section we utilize an analytical perturbative approach, originally developed by Greffet for calculating the scattered electromagnetic waves above a rough dielectric surface,[26] in order to obtain the required Green's dyadics $\mathbb{G}_r^E$ and $\mathbb{G}_r^H$. Greffet's approach results in a series of recursively determined contributions in ascending orders of the surface profile, and thus enables one to systematically assess the higher-order terms.

A. Calculational scheme

We assume that the surface is described by an expression $z=hf(x,y)$, where $f(x,y)$ is a normalized function varying between +1 and −1; the scaling parameter h carries the dimension of a length. The nonmagnetic dielectric medium, equipped with permittivity $\epsilon(\omega)$, fills the entire half space $z<hf(x,y)$. For $z>hf(x,y)$, outside the dielectric, the total electric field consists of a prescribed incident component $\boldsymbol{E}_i(\boldsymbol{r})$, and of the so far unknown reflected component $\boldsymbol{E}_r(\boldsymbol{r})$, while the transmitted field inside the dielectric is denoted as $\boldsymbol{E}_t(\boldsymbol{r})$. Greffet has given a recursive series solution for the transmitted and the reflected field,[26] invoking the extinction theorem and the Rayleigh hypothesis.[29] The extinction theorem amounts to an exact integral formulation of the boundary condition, whereas the use of the Rayleigh hypothesis means expanding the transmitted, incident, and reflected fields in plane waves traveling in z direction,

$$\boldsymbol{E}_t(\boldsymbol{r}) = \int d^2\kappa \boldsymbol{e}_t(\boldsymbol{\kappa}) e^{i(\boldsymbol{\kappa}\cdot\boldsymbol{\rho}-k_z z)}, \tag{6}$$

$$\boldsymbol{E}_i(\boldsymbol{r}) = \int d^2\kappa \boldsymbol{e}_i(\boldsymbol{\kappa}) e^{i(\boldsymbol{\kappa}\cdot\boldsymbol{\rho}-k_{z0} z)}, \tag{7}$$

and

$$\boldsymbol{E}_r(\boldsymbol{r}) = \int d^2\kappa \boldsymbol{e}_r(\boldsymbol{\kappa}) e^{i(\boldsymbol{\kappa}\cdot\boldsymbol{\rho}+k_{z0} z)}. \tag{8}$$

Here we write $\boldsymbol{r}=[x,y,z]^t$ for the position vector, $\boldsymbol{\rho}=[x,y,0]^t$ for its lateral part, and $\boldsymbol{\kappa}=[k_x,k_y,0]^t$ for the lateral component of the wave vector; moreover,

$$k_z = \sqrt{\epsilon k_0 - \kappa} \tag{9}$$

and

$$k_{z0} = \sqrt{k_0 - \kappa} \tag{10}$$

are the z components of the wave vector inside and outside the medium. We also use the notation $k_0=\omega/c$ and $\kappa=|\boldsymbol{\kappa}|$. These expansions (6)–(8) assume translational symmetry in the x-y plane and hence are strictly justified outside the structured region, that is, for $z>h$ and $z<-h$. However, the extinction theorem requires to evaluate the fields on the very surface of the dielectric, where the validity of the above expressions cannot be taken for granted. Ignoring this complication and using the expansions (6)–(8) nonetheless is a common procedure[30,31] which has been looked into by several authors from the mathematical point of view;[32–35] it appears to work reliably at least for sufficiently small values of h. For example, in the case of a sinusoidal grating described by $z=(h/2)\cos(2\pi x/D)$ this Rayleigh hypothesis holds rigorously[32–34] up to $h_{\max}/D=0.142521$, and may therefore be employed for both the propagating and the evanescent parts of the field as long as the ratio h/D stays below this boundary.

The field's Fourier components then are expanded in the forms

$$\boldsymbol{e}_t(\boldsymbol{\kappa}) = \sum_{m=0}^{\infty} \frac{\boldsymbol{e}_t^{(m)}(\boldsymbol{\kappa})}{m!}, \tag{11}$$

$$\boldsymbol{e}_r(\boldsymbol{\kappa}) = \sum_{m=0}^{\infty} \frac{\boldsymbol{e}_r^{(m)}(\boldsymbol{\kappa})}{m!}, \tag{12}$$

and

$$\boldsymbol{e}_i(\boldsymbol{\kappa}) = \sum_{m=0}^{\infty} \frac{\boldsymbol{e}_i^{(m)}(\boldsymbol{\kappa})}{m!} = \boldsymbol{e}_i^{(0)}(\boldsymbol{\kappa}). \tag{13}$$

It is useful to split the fields into their s and p components according to

$$\boldsymbol{e}_{\mathrm{t}}(\boldsymbol{\kappa}) = e_{\mathrm{t,s}}(\boldsymbol{\kappa})\boldsymbol{a}_{\mathrm{s}}(\boldsymbol{\kappa}) + e_{\mathrm{t,p}}(\boldsymbol{\kappa})\boldsymbol{a}^{-}_{\mathrm{p,t}}(\boldsymbol{\kappa}), \tag{14}$$

$$\boldsymbol{e}_{\mathrm{i}}(\boldsymbol{\kappa}) = e_{\mathrm{i,s}}(\boldsymbol{\kappa})\boldsymbol{a}_{\mathrm{s}}(\boldsymbol{\kappa}) + e_{\mathrm{i,p}}(\boldsymbol{\kappa})\boldsymbol{a}^{-}_{\mathrm{p,0}}(\boldsymbol{\kappa}), \tag{15}$$

and

$$\boldsymbol{e}_{\mathrm{r}}(\boldsymbol{\kappa}) = e_{\mathrm{r,s}}(\boldsymbol{\kappa})\boldsymbol{a}_{\mathrm{s}}(\boldsymbol{\kappa}) + e_{\mathrm{r,p}}(\boldsymbol{\kappa})\boldsymbol{a}^{+}_{\mathrm{p,0}}(\boldsymbol{\kappa}), \tag{16}$$

where

$$\boldsymbol{a}_{\mathrm{s}}(\boldsymbol{\kappa}) = \frac{1}{\kappa}\begin{bmatrix} -k_y \\ k_x \\ 0 \end{bmatrix}, \tag{17}$$

$$\boldsymbol{a}^{-}_{\mathrm{p,t}}(\boldsymbol{\kappa}) = -\frac{1}{nk_0\kappa}\begin{bmatrix} k_x k_z \\ k_y k_z \\ \kappa^2 \end{bmatrix}, \tag{18}$$

$$\boldsymbol{a}^{-}_{\mathrm{p,0}}(\boldsymbol{\kappa}) = -\frac{1}{k_0\kappa}\begin{bmatrix} k_x k_{z0} \\ k_y k_{z0} \\ \kappa^2 \end{bmatrix}, \tag{19}$$

and

$$\boldsymbol{a}^{+}_{\mathrm{p,0}}(\boldsymbol{\kappa}) = \frac{1}{k_0\kappa}\begin{bmatrix} k_x k_{z0} \\ k_y k_{z0} \\ -\kappa^2 \end{bmatrix}, \tag{20}$$

here $n=\sqrt{\epsilon}$ is the index of refraction.

Following Greffet,[26] one then obtains the transmitted field in the recursive form

$$\begin{bmatrix} e^{(m)}_{\mathrm{t,s}}(\boldsymbol{\kappa}) \\ e^{(m)}_{\mathrm{t,p}}(\boldsymbol{\kappa}) \end{bmatrix} = \frac{k_z - k_{z0}}{4\pi^2}\mathbb{R}^{-1}(\boldsymbol{\kappa},\boldsymbol{\kappa})\int d^2\kappa' \Bigg\{ \mathbb{R}(\boldsymbol{\kappa},\boldsymbol{\kappa}') \times \sum_{q=1}^{m}\binom{m}{q}\frac{(ih)^q \hat{F}^{(q)}(\boldsymbol{\kappa}'-\boldsymbol{\kappa})}{(k_{z0}-k'_z)^{1-q}}\begin{bmatrix} e^{(m-q)}_{\mathrm{t,s}}(\boldsymbol{\kappa}') \\ e^{(m-q)}_{\mathrm{t,p}}(\boldsymbol{\kappa}') \end{bmatrix}\Bigg\} \tag{21}$$

so that $\boldsymbol{e}^{(m)}_{\mathrm{t}}(\boldsymbol{\kappa})$ is proportional to h^m; the according expression for the reflected field reads

$$\begin{bmatrix} e^{(m)}_{\mathrm{r,s}}(\boldsymbol{\kappa}) \\ e^{(m)}_{\mathrm{r,p}}(\boldsymbol{\kappa}) \end{bmatrix} = \frac{\epsilon - 1}{8\pi^2 k_{z0}}\Bigg\{ \int d^2\kappa' \Bigg(\mathbb{P}(\boldsymbol{\kappa},\boldsymbol{\kappa}') \times \sum_{q=0}^{m-1}\binom{m}{q}\frac{(-ih)^{m-q}\hat{F}^{(m-q)}(\boldsymbol{\kappa}'-\boldsymbol{\kappa})}{(k_{z0}+k'_z)^{1+q-m}} \times \begin{bmatrix} e^{(q)}_{\mathrm{t,s}}(\boldsymbol{\kappa}') \\ e^{(q)}_{\mathrm{t,p}}(\boldsymbol{\kappa}') \end{bmatrix}\Bigg) + \mathbb{P}(\boldsymbol{\kappa},\boldsymbol{\kappa})\frac{4\pi^2}{k_z + k_{z0}}\begin{bmatrix} e^{(m)}_{\mathrm{t,s}}(\boldsymbol{\kappa}) \\ e^{(m)}_{\mathrm{t,p}}(\boldsymbol{\kappa}) \end{bmatrix}\Bigg\}. \tag{22}$$

In these equations the quantities $\hat{F}^{(n)}(\boldsymbol{\kappa})$ denote the Fourier transforms of powers of the surface function,

$$\hat{F}^{(n)}(\boldsymbol{\kappa}) = \int d^2\rho e^{i\boldsymbol{\kappa}\cdot\boldsymbol{\rho}} f^n(\boldsymbol{\rho}). \tag{23}$$

The linear operators $\mathbb{R}(\boldsymbol{\kappa},\boldsymbol{\kappa}')$ and $\mathbb{P}(\boldsymbol{\kappa},\boldsymbol{\kappa}')$ effectuate the double vectorial product with $\boldsymbol{k}^{-}_{\mathrm{r}}=[k_x,k_y,-k_{z0}]^t$ and $\boldsymbol{k}^{+}_{\mathrm{r}}=[k_x,k_y,k_{z0}]^t$, respectively; these double products (namely, $\boldsymbol{k}^{-}_{\mathrm{r}}\times\boldsymbol{k}^{-}_{\mathrm{r}}\times$ and $\boldsymbol{k}^{+}_{\mathrm{r}}\times\boldsymbol{k}^{+}_{\mathrm{r}}\times$) typically appear when using the extinction theorem. In the basis chosen, the matrix forms of these operators are

$$\mathbb{R}(\boldsymbol{\kappa},\boldsymbol{\kappa}') = -\frac{k_0^2}{\kappa\kappa'}\begin{bmatrix} \boldsymbol{\kappa}\cdot\boldsymbol{\kappa}' & -\dfrac{k'_z(\boldsymbol{\kappa}\times\boldsymbol{\kappa}')_z}{nk_0} \\ \dfrac{k_{z0}(\boldsymbol{\kappa}\times\boldsymbol{\kappa}')_z}{k_0} & \dfrac{\kappa^2\kappa'^2 + \boldsymbol{\kappa}\cdot\boldsymbol{\kappa}' k_{z0}k'_z}{nk_0^2} \end{bmatrix} \tag{24}$$

and

$$\mathbb{P}(\boldsymbol{\kappa},\boldsymbol{\kappa}') = -\frac{k_0^2}{\kappa\kappa'}\begin{bmatrix} \boldsymbol{\kappa}\cdot\boldsymbol{\kappa}' & -\dfrac{k'_z(\boldsymbol{\kappa}\times\boldsymbol{\kappa}')_z}{nk_0} \\ -\dfrac{k_{z0}(\boldsymbol{\kappa}\times\boldsymbol{\kappa}')_z}{k_0} & \dfrac{\kappa^2\kappa'^2 - \boldsymbol{\kappa}\cdot\boldsymbol{\kappa}' k_{z0}k'_z}{nk_0^2} \end{bmatrix}, \tag{25}$$

writing $(\boldsymbol{\kappa}\times\boldsymbol{\kappa}')_z$ for the z component of the vectorial product of $\boldsymbol{\kappa}$ and $\boldsymbol{\kappa}'$.

The above recursions start from the well-known half-space results obtained for a perfectly flat surface, which can be cast into the forms

$$\begin{bmatrix} e^{(0)}_{\mathrm{t,s}}(\boldsymbol{\kappa}) \\ e^{(0)}_{\mathrm{t,p}}(\boldsymbol{\kappa}) \end{bmatrix} = \begin{bmatrix} t_{\mathrm{s}}(\boldsymbol{\kappa}) & 0 \\ 0 & t_{\mathrm{p}}(\boldsymbol{\kappa}) \end{bmatrix}\begin{bmatrix} e_{\mathrm{i,s}}(\boldsymbol{\kappa}) \\ e_{\mathrm{i,p}}(\boldsymbol{\kappa}) \end{bmatrix} \tag{26}$$

and

$$\begin{bmatrix} e^{(0)}_{\mathrm{r,s}}(\boldsymbol{\kappa}) \\ e^{(0)}_{\mathrm{r,p}}(\boldsymbol{\kappa}) \end{bmatrix} = \begin{bmatrix} r_{\mathrm{s}}(\boldsymbol{\kappa}) & 0 \\ 0 & r_{\mathrm{p}}(\boldsymbol{\kappa}) \end{bmatrix}\begin{bmatrix} e_{\mathrm{i,s}}(\boldsymbol{\kappa}) \\ e_{\mathrm{i,p}}(\boldsymbol{\kappa}) \end{bmatrix} \tag{27}$$

with the Fresnel coefficients

$$t_{\mathrm{s}}(\boldsymbol{\kappa}) = \frac{2k_{z0}}{k_{z0}+k_z}; \quad t_{\mathrm{p}}(\boldsymbol{\kappa}) = \frac{2nk_{z0}}{n^2k_{z0}+k_z},$$

$$r_{\mathrm{s}}(\boldsymbol{\kappa}) = \frac{k_{z0}-k_z}{k_{z0}+k_z}; \quad r_{\mathrm{p}}(\boldsymbol{\kappa}) = \frac{n^2k_{z0}-k_z}{n^2k_{z0}+k_z}.$$

From these fields (21) and (22) we now proceed to the calculation of the Green's dyadics. More precisely, in order to compute the local density of states we need to determine the reflected part of the Green's dyadics for coinciding source and observation points. To this end, we take the field of a deltalike source current located at $\boldsymbol{\rho}+z\boldsymbol{e}_z$ and pointing into the direction of the unit vector $\boldsymbol{j}$ as incident field, giving

$$\begin{bmatrix} e_{\mathrm{i,s}}(\boldsymbol{\kappa}) \\ e_{\mathrm{i,p}}(\boldsymbol{\kappa}) \end{bmatrix} = -\frac{\omega\mu_0}{2k_{z0}}e^{-i(\boldsymbol{\kappa}\cdot\boldsymbol{\rho}-k_{z0}z)}\begin{bmatrix} \boldsymbol{a}_{\mathrm{s}}(\boldsymbol{\kappa})\cdot\boldsymbol{j} \\ \boldsymbol{a}^{-}_{\mathrm{p,0}}(\boldsymbol{\kappa})\cdot\boldsymbol{j} \end{bmatrix}. \tag{28}$$

To zeroth order in h, the reflected field then is

$$\begin{bmatrix} e_{\mathrm{r,s}}^{(0)}(\boldsymbol{\kappa}) \\ e_{\mathrm{r,p}}^{(0)}(\boldsymbol{\kappa}) \end{bmatrix} = -\frac{\omega\mu_0}{2k_{z0}} e^{-i(\boldsymbol{\kappa}\cdot\boldsymbol{\rho}-k_{z0}z)} \begin{bmatrix} r_{\mathrm{s}}(\boldsymbol{\kappa}) & 0 \\ 0 & r_{\mathrm{p}}(\boldsymbol{\kappa}) \end{bmatrix} \begin{bmatrix} \boldsymbol{a}_{\mathrm{s}}(\boldsymbol{\kappa})\cdot\boldsymbol{j} \\ \boldsymbol{a}_{\mathrm{p},0}^{+}(\boldsymbol{\kappa})\cdot\boldsymbol{j} \end{bmatrix}. \tag{29}$$

The directions of the s and p components of the incident field are given by $\boldsymbol{a}_{\mathrm{s}}(\boldsymbol{\kappa})$ and $\boldsymbol{a}_{\mathrm{p},0}^{-}(\boldsymbol{\kappa})$, while the components of the reflected field are given by $\boldsymbol{a}_{\mathrm{s}}(\boldsymbol{\kappa})$ and $\boldsymbol{a}_{\mathrm{p},0}^{+}(\boldsymbol{\kappa})$. Therefore it is convenient to split the Fourier coefficients of the Green's dyadics into the four parts that result from taking the dyadic products of these unit vectors, leading to

$$\begin{aligned} g_{\mathrm{r}}^{\mathrm{E},(0)}(\boldsymbol{\kappa}) = {} & g_{\mathrm{r,ss}}^{\mathrm{E},(0)}(\boldsymbol{\kappa})\boldsymbol{a}_{\mathrm{s}}(\boldsymbol{\kappa}) \otimes \boldsymbol{a}_{\mathrm{s}}(\boldsymbol{\kappa}) + g_{\mathrm{r,sp}}^{\mathrm{E},(0)}(\boldsymbol{\kappa})\boldsymbol{a}_{\mathrm{s}}(\boldsymbol{\kappa}) \otimes \boldsymbol{a}_{\mathrm{p},0}^{-}(\boldsymbol{\kappa}) \\ & + g_{\mathrm{r,ps}}^{\mathrm{E},(0)}(\boldsymbol{\kappa})\boldsymbol{a}_{\mathrm{p},0}^{+}(\boldsymbol{\kappa}) \otimes \boldsymbol{a}_{\mathrm{s}}(\boldsymbol{\kappa}) \\ & + g_{\mathrm{r,pp}}^{\mathrm{E},(0)}(\boldsymbol{\kappa})\boldsymbol{a}_{\mathrm{p},0}^{+}(\boldsymbol{\kappa}) \otimes \boldsymbol{a}_{\mathrm{p},0}^{-}(\boldsymbol{\kappa}). \end{aligned} \tag{30}$$

Having employed a deltalike source current the relation between the field and the electric Green's dyadic simply reads $\mathbb{G}^{\mathrm{E}}\cdot\boldsymbol{j}=\boldsymbol{E}/(i\omega\mu_0)$, so that the coefficients of this dyadic can easily be read off from Eq. (29). By means of an inverse Fourier transform, equating source and observation point, one then arrives at the familiar result for the reflected Green's dyadic pertaining to a flat surface,

$$\begin{aligned} \mathbb{G}_{\mathrm{r}}^{\mathrm{E},(0)} = {} & \frac{i}{4\pi^2}\int d^2\kappa \frac{e^{2ik_{z0}z}}{2k_{z0}}[r_{\mathrm{s}}(\boldsymbol{\kappa})\boldsymbol{a}_{\mathrm{s}}(\boldsymbol{\kappa}) \otimes \boldsymbol{a}_{\mathrm{s}}(\boldsymbol{\kappa}) \\ & + r_{\mathrm{p}}(\boldsymbol{\kappa})\boldsymbol{a}_{\mathrm{p},0}^{+}(\boldsymbol{\kappa}) \otimes \boldsymbol{a}_{\mathrm{p},0}^{-}(\boldsymbol{\kappa})]. \end{aligned} \tag{31}$$

With the help of Eq. (22) one obtains similar expressions to all orders in the profile height h. An advantage of this approach lies in the fact that it is then quite easy to also determine the magnetic Green's dyadic, which is related to the electric one through[36]

$$\mathbb{G}_{\mathrm{r}}^{\mathrm{H}}(\boldsymbol{r},\boldsymbol{r}) = -\frac{1}{k_0^2}\nabla \times \mathbb{G}_{\mathrm{r}}^{\mathrm{E}}(\boldsymbol{r},\boldsymbol{r}') \times \nabla'|_{\boldsymbol{r}'=\boldsymbol{r}}. \tag{32}$$

In Fourier space the operator ∇ is replaced either by $i(\boldsymbol{\kappa}+k_{z0}\boldsymbol{e}_z)$ or by $-i(\boldsymbol{\kappa}-k_{z0}\boldsymbol{e}_z)$, depending on whether the curl acts on a unit vector belonging to the incident or to the reflected field. Therefore, the magnetic Green's dyadic is derived from its electric counterpart by simply replacing $\boldsymbol{a}(\boldsymbol{\kappa})\otimes\boldsymbol{a}(\boldsymbol{\kappa}')$ by the expression $-\frac{1}{k_0^2}(\boldsymbol{\kappa}+k_{z0}\boldsymbol{e}_z)\times\boldsymbol{a}(\boldsymbol{\kappa})\otimes\boldsymbol{a}(\boldsymbol{\kappa}')\times(\boldsymbol{\kappa}'-k'_{z0}\boldsymbol{e}_z)$. Here we introduce $\boldsymbol{\kappa}'$ and k'_{z0} because it is only to zeroth order that the reflected and the incident field are characterized by the same wave vector.

Finally, for calculating the trace of the Green's dyadics one just has to replace the dyadic products by their traces. Hence, the method sketched here yields a transparent strategy for obtaining the electric and the magnetic LDOS above a structured surface. In practice, a restriction on the maximum order achievable is imposed by the available computational resources. To zeroth order only two-dimensional integrals have to be evaluated, to first-order four-dimensional integrals appear; to second order one already has to deal with six-dimensional integrals, and so on. Clearly, a good choice of the numerical tools is decisive here; we therefore present some details of our implementation.

B. Numerical implementation

We exemplarily discuss the calculation of the electric local density of states to first and second orders; its magnetic counterpart, and the higher-order terms, are determined in a similar way. With the help of Eq. (22) the trace of the first-order contribution to the electric reflected Green's dyadic is computed as

$$\mathrm{Tr}\{\mathbb{G}_{\mathrm{r}}^{\mathrm{E},(1)}\} = -\int \frac{d^2q}{4\pi^2} e^{i\boldsymbol{q}\cdot\boldsymbol{\rho}}\hat{F}^{(1)}(-\boldsymbol{q})a_1(\boldsymbol{q}), \tag{33}$$

where $a_1(\boldsymbol{q})$ is given by the integral

$$a_1(\boldsymbol{q}) = \int d^2\kappa' \boldsymbol{S}^{(1)}(\boldsymbol{q}+\boldsymbol{\kappa}',\boldsymbol{\kappa}')\cdot\boldsymbol{A}_{\mathrm{tr}}^{(\mathrm{E})}(\boldsymbol{q}+\boldsymbol{\kappa}',\boldsymbol{\kappa}') \tag{34}$$

with the four-dimensional vectors $\boldsymbol{S}^{(1)}$ and $\boldsymbol{A}_{\mathrm{tr}}^{(\mathrm{E})}$ specified in the Appendix. We either employ an experimentally determined surface profile,[12] or some suitably selected model function $f(\boldsymbol{\rho})$; sample it, and perform a discrete FFT in order to determine $\hat{F}^{(1)}$. Then we compute $a(\boldsymbol{q})$ for each required $\boldsymbol{q}$ by numerical integration, and finally take an inverse FFT of $\hat{F}^{(1)}(-\boldsymbol{q})a(\boldsymbol{q})$ to get the trace (33) of the first-order Green's dyadic.

To second order one has to deal with two contributions, one containing $\hat{F}^{(2)}$, the other feeding from two factors $\hat{F}^{(1)}$. The former contribution has the same structure as the first-order term,

$$\mathrm{Tr}\{\mathbb{G}_{\mathrm{r},1}^{\mathrm{E},(2)}\} = \int \frac{d^2q}{4\pi^2} e^{i\boldsymbol{q}\cdot\boldsymbol{\rho}}\hat{F}^{(2)}(-\boldsymbol{q})a_2(\boldsymbol{q}) \tag{35}$$

with

$$a_2(\boldsymbol{q}) = \int d^2\kappa' \boldsymbol{S}_1^{(2)}(\boldsymbol{q}+\boldsymbol{\kappa}',\boldsymbol{\kappa}')\cdot\boldsymbol{A}_{\mathrm{tr}}^{(\mathrm{E})}(\boldsymbol{q}+\boldsymbol{\kappa}',\boldsymbol{\kappa}') \tag{36}$$

and is evaluated in the same manner. The other contribution contains a further integral,

$$\begin{aligned} \mathrm{Tr}\{\mathbb{G}_{\mathrm{r},2}^{\mathrm{E},(2)}\} = {} & \int \frac{d^2q}{4\pi^2} e^{i\boldsymbol{q}\cdot\boldsymbol{\rho}}\hat{F}^{(1)}(-\boldsymbol{q}) \int \frac{d^2q'}{4\pi^2} e^{i\boldsymbol{q}'\cdot\boldsymbol{\rho}} \\ & \times \hat{F}^{(1)}(-\boldsymbol{q}')a_3(\boldsymbol{q},\boldsymbol{q}') \end{aligned} \tag{37}$$

with integration variables $\boldsymbol{q}=\boldsymbol{\kappa}-\boldsymbol{\kappa}'$ and $\boldsymbol{q}'=\boldsymbol{\kappa}'-\boldsymbol{\kappa}''$, and with the expression

$$a_3(\boldsymbol{q},\boldsymbol{q}') = \int d^2\kappa'' e^{i(k_{z0}+k''_{z0})z}\boldsymbol{S}_2^{(2)}(\boldsymbol{\kappa},\boldsymbol{\kappa}',\boldsymbol{\kappa}'')\cdot\boldsymbol{A}_{\mathrm{tr}}^{(\mathrm{E})}(\boldsymbol{\kappa},\boldsymbol{\kappa}''), \tag{38}$$

again, $\boldsymbol{S}_1^{(2)}$ and $\boldsymbol{S}_2^{(2)}$ are stated explicitly in the Appendix. After computing $a_3(\boldsymbol{q},\boldsymbol{q}')$ on a discrete mesh of $\boldsymbol{q}$ and $\boldsymbol{q}'$, a four-dimensional inverse FFT is performed for determining the resulting contribution to the trace of the Green's dyadic.

The integrals are numerically evaluated using Cuba routines;[37] the Fourier transforms are executed by means of the FFTW library.[38]

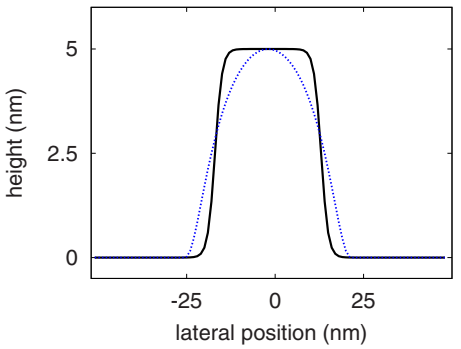

FIG. 1. (Color online) Profile function (39) with parameters as employed in our model calculations, height $h=5$ nm, width $w=30$ nm, and inverse smoothing length $\zeta=10^9$ m^{-1} (full line), together with the reference profile (40) (dashed). In either case, the dielectric properties of the sample are given by the Drude model with parameters for gold at 300 K.

III. RESULTS

In this section we discuss some numerical results for the local density of states above example topographies, calculated to second order in the profile height. We first consider the relative magnitude of the individual contributions, in order to estimate under which conditions the termination of the perturbation series can be justified. We then use the second-order data to discuss the resolution power of an idealized NSThM in a mode of operation in which the total heat transfer is kept constant while scanning a sample's surface.

A. Magnitude of second-order contributions

Our basic model structure is a bar with height h and smoothed edges placed on an otherwise perfectly planar surface, infinitely extended in y direction and possessing the width w in x direction, as described by the function

$$hf_1(x) = h\frac{1}{\exp[\zeta(|x| - 0.5w)] + 1}. \tag{39}$$

Our calculations are done for $h=5$ nm, $w=30$ nm, and inverse smoothing length $\zeta=10^9$ m^{-1}. For comparison, we also consider the somewhat rounder profile

$$hf_1(x) = h\exp\left(-\frac{1}{1-(x/v)^2}+1\right) \tag{40}$$

with v adjusted such that the respective areas under the two functions (39) and (40) coincide. The resulting profile shapes are drawn in Fig. 1.

Because these profiles depend on only one variable, the Fourier transforms $\hat{F}^{(n)}$ contain delta functions, so that the integrals over q and q' in Eqs. (33), (35), and (37) become effectively one-dimensional, drastically reducing the numerical effort. The profiles are discretized with a stepsize of 1 nm, covering a total range of 500 nm; we have checked that the numerical results thus obtained are stable against further reduction of the grid size to 0.5nm. We assume that the dielectric function $\epsilon(\omega)$ of the samples is given by the Drude model[39]

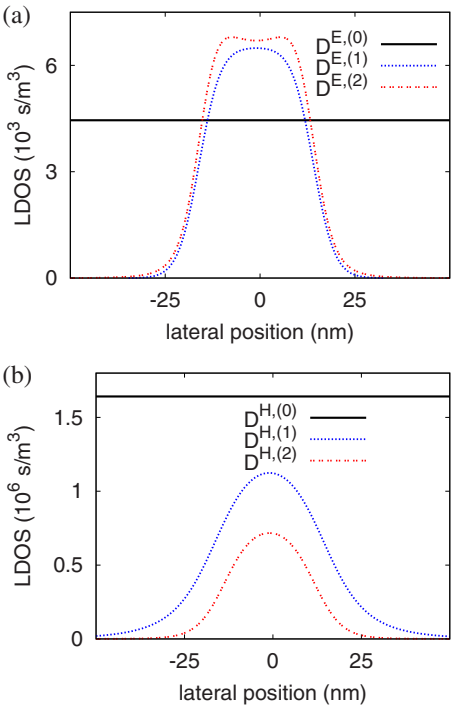

FIG. 2. (Color online) Zeroth-, first-, and second-order contributions to the (a) electric and to the (b) magnetic parts of the LDOS above a gold surface structured with the nanobar (39) as sketched in Fig. 1, for $\omega=10^{14}$ s^{-1} at an observation height of 10 nm above the base substrate plane. Note the different scales.

$$\varepsilon(\omega) = 1 - \frac{\omega_p^2}{\omega^2 + i\gamma\omega} \tag{41}$$

with plasma frequency $\omega_p=1.4\times10^{16}$ s^{-1} and inverse relaxation time $\gamma=3.3\times10^{13}$ s^{-1}, describing gold at the temperature $T=300$ K.

In Fig. 2 we depict the zeroth-, first-, and second-order contributions to the electric and to the magnetic part of the LDOS for the structure (39), evaluated at a constant height of 10 nm above the base plane for $\omega=10^{14}$ s^{-1}, roughly equal to the dominant thermal frequency at 300 K. The second-order terms qualitatively show the same behavior as the first-order ones,[27] but there is a notable difference between the electric and the magnetic part. The second-order contribution to the magnetic LDOS at least is smaller than its first-order precessor, although only by a factor which is not small compared to unity, whereas the magnitude of the second-order electric contribution remains comparable to that of the first-order one, and even slightly exceeds it. At the bar's center, the first- and the second-order electric contributions amount to roughly 1.5 times the zero-order term. This behavior is not accidental; it can be quantitatively understood with the help of an elementary consideration. At sufficiently short distances, that is, for $z-h$ not too large compared to the profile width w, the local geometry equals that of a flat surface, shifted by h against the base plane. Therefore, the electric LDOS D^E at such a point $\boldsymbol{r}=[0,0,z]^t$ is approximately given by the LDOS D^E_{fs} pertaining to a perfectly flat surface[19] through the relation

$$D^{\mathrm{E}}(\boldsymbol{r}) \approx D^{\mathrm{E}}_{\mathrm{fs}}([0,0,z-h]^t). \tag{42}$$

Now the distance dependence of $D^{\mathrm{E}}_{\mathrm{fs}}$ in the near field is given by

$$D^{\mathrm{E}}_{\mathrm{fs}}([0,0,z]^t) \sim \frac{1}{z^3}, \tag{43}$$

the strong decay of this electric LDOS with the third power of the distance clearly aids the local approximation Eq. (42). Thus, one has

$$D^{\mathrm{E}}([0,0,z]^t) \sim \frac{1}{(z-h)^3}. \tag{44}$$

Expanding in powers of h, this yields

$$D^{\mathrm{E}}([0,0,z]^t) \sim \frac{1}{z^3} + \frac{3h}{z^4} + \frac{6h^2}{z^5} + O(h^3), \tag{45}$$

allowing one to estimate the ratios of the contributions appearing in different orders:

$$\frac{D^{\mathrm{E},(1)}}{D^{\mathrm{E},(0)}} \approx 3\frac{h}{z}; \quad \frac{D^{\mathrm{E},(2)}}{D^{\mathrm{E},(0)}} \approx 6\frac{h^2}{z^2}. \tag{46}$$

With $h/z=0.5$, which is the value considered in Fig. 2, one obtains $D^{\mathrm{E},(1)}/D^{\mathrm{E},(0)}=D^{\mathrm{E},(2)}/D^{\mathrm{E},(0)}=1.5$, in quite good agreement with the exact numerical result. Generalizing this argument to any order n, one observes

$$\frac{D^{\mathrm{E},(n+1)}}{D^{\mathrm{E},(n)}} \approx \frac{n+3}{n+1}\frac{h}{z}. \tag{47}$$

Thus, while the series may still converge for any $z>h$, convergence at short distances would be rather slow; for $h/z=0.5$ the magnitude of the leading successive contributions, normalized to the zeroth-order one, is 1:3/2:3/2:5/4:15/16:21/32:…. In this example, terminating the perturbation series at the second order means that one collects only about half of the exact value.

In the case of the magnetic LDOS, one has

$$D^{\mathrm{H}}_{\mathrm{fs}}([0,0,z]^t) \sim \frac{1}{z} \tag{48}$$

so that here a larger area of the sample's surface contributes to the LDOS than in the electric case (43), implying that a local approximation analogous to Eq. (42) cannot be expected to work as well as before. Ignoring this restriction and performing the analysis nonetheless, one ends up with

$$\frac{D^{\mathrm{H},(n+1)}}{D^{\mathrm{H},(n)}} \approx \frac{h}{z}, \tag{49}$$

which, in view of the shaky foundation of the reasoning, still works satisfactorily, capturing both the correct trends and the orders of magnitude read off from Fig. 2.

It is evident that these general findings do *not* depend on the specific dielectric properties of the material. Indeed, when considering a polar sample with a permittivity described by the Reststrahlen formula[40]

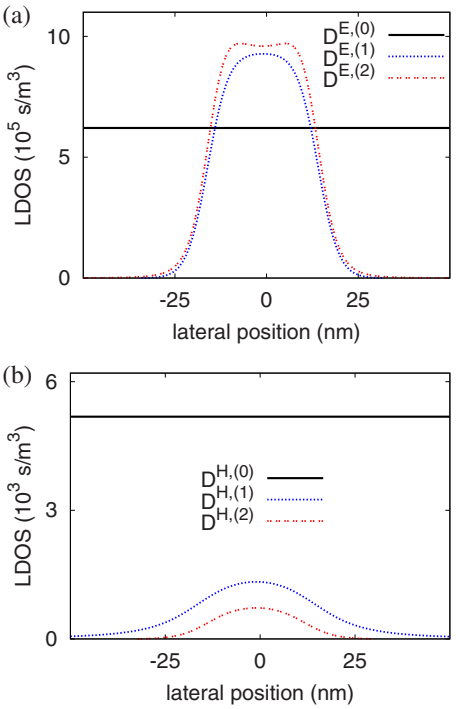

FIG. 3. (Color online) As Fig. 2, but for a sample consisting of gallium nitride (GaN).

$$\epsilon(\omega) = \epsilon_\infty\left(1 + \frac{\omega_{\mathrm{L}}^2 - \omega_{\mathrm{T}}^2}{\omega_{\mathrm{T}}^2 - \omega^2 - i\gamma\omega}\right) \tag{50}$$

and inserting parameters appropriate for gallium nitride,[41] namely, $\epsilon_\infty=5.35$ for the high-frequency permittivity, $\omega_{\mathrm{L}}=1.41\times10^{14}$ s^{-1} and $\omega_{\mathrm{T}}=1.06\times10^{14}$ s^{-1} for the frequencies of the longitudinal and transversal phonons, and $\gamma=1.51\times10^{12}$ s^{-1} for the relaxation rate, and again taking the profile Eq. (39), we obtain Fig. 3, which shows the same qualitative features as the previous Fig. 2 for the gold sample, although, of course, the scales are quite different; now the electric contribution dominates. Likewise, the results do not seem to depend sensitively on the precise form of the structure. The corresponding data obtained for the reference profile (40) are remarkably similar to the previous ones, as shown in Fig. 4, and again confirm the simple estimates (47) and (49). For this reason, we only consider the gold nanobar (39) in the following.

To conclude the above discussion, in the cases studied so far the restriction to second-order perturbation theory already seems questionable, although the strong dominance of the magnetic LDOS for metallic samples might still mask the problem with the electric one. This is potentially important for NSThM-applications, where typical probe-sample distances range down to a few nanometers. On the other hand, low-order perturbation theory may be expected to work reliably when the profile height h clearly is the smallest length scale of the problem; according to the above reasoning, it should become better when increasing the observation distance z. In order to estimate the smallest z at which second-order perturbation theory might still give quantitatively good results for our model profile (39), we plot in Fig. 5 the ratios

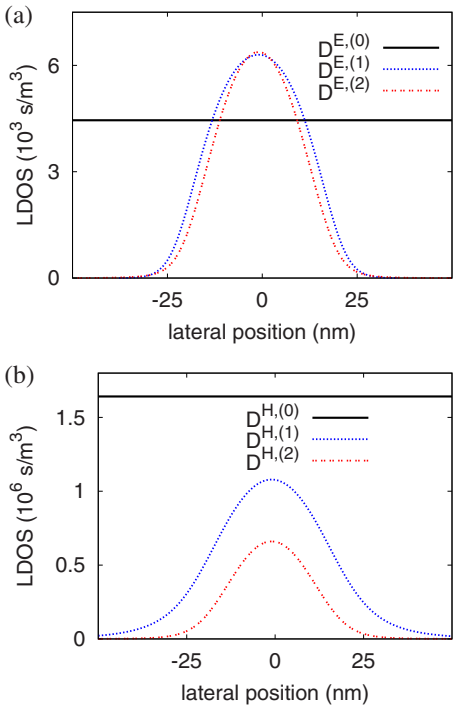

FIG. 4. (Color online) As Fig. 2, for a gold sample with the reference profile (40).

of the various contributions, evaluated above the bar's center at varying distance; here we also consider the regime $z-h \gg w$ where the short-distance estimates (47) and (49) may no longer be taken for granted. As a rough guideline, one

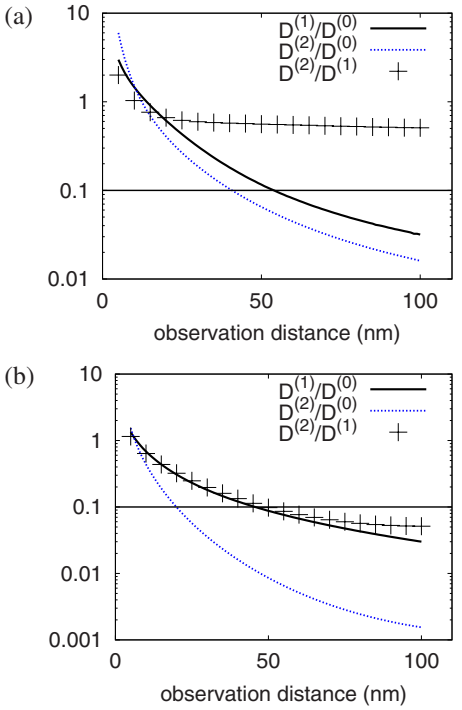

FIG. 5. (Color online) Ratios of the zeroth-, first-, and second-order contributions to the (a) electric and to the (b) magnetic LDOS for $\omega=10^{14}$ s^{-1} at an observation point $x=0$ above the center of the bar (39).

may accept the truncation of the perturbation series at the second order if the ratio of the second-order contribution to the zeroth-order one drops below 10%, say. For the dominant magnetic part this criterion is satisfied for $z>20$ nm, while the electric part then requires $z>41$ nm. (When reducing the acceptance limit to 5%, one gets $z>26$ nm and $z>56$ nm, respectively.) The potential problem of slow convergence here is expressed by the fact that the ratio of second- to first-order contribution decreases only rather slowly with increasing z. Still, in view of the relative smallness of the electric LDOS above metallic samples this does not seem to be essential.

B. Resolution of an NSThM

Scanning the LDOS at a constant height above the base plane, as done numerically in Figs. 2–4, corresponds to the *constant height* mode of operation of an NSThM. This is not an advantageous mode, for two practical reasons. On the one hand, it is hard to realize with sufficient accuracy, on the other, it contains the risk of a probe-sample collision when scanning a surface with an unknown topography, almost always resulting in irreparable damage to the delicate sensor.[11] A much more favorable mode avoiding these complications is the *constant transfer* mode, meaning that the sensor height is continuously regulated such that the detected heat current remains constant when moving the sensor over the surface; the information about the sample's near field then is embodied in the recorded sensor height. Note that this latter mode differs from the *constant distance* mode, which uses additional information on the local distance of the sensor from the structured surface (obtained by electron tunneling spectroscopy) in order to keep that distance constant. That constant distance mode was employed experimentally by Kittel *et al.*;[12] numerical first-order results pertaining to this mode can be found in Ref. 27. In contrast, a major benefit of the constant transfer mode lies in the fact that it exclusively requires heat-transfer information, so that there is no need to retain the sensor's ordinary STM-capability. Moreover, it allows one to assess the resolution limit of the NSThM in a simple manner.

For modeling this constant transfer mode, we select some appropriate fixed value of the LDOS, and then calculate that observation distance a at which this LDOS-value is reached. Only the sum of all contributions is of interest now. For consistency, we also require that the second-order to zeroth-order ratio remains less than 10% for the magnetic LDOS, as the electric one does not contribute significantly here. Discussing the NSThM's resolution power first requires the specification of a norm structure containing the length scale s to be resolved. Here we take two parallel gold bars of the form (39), as described by the profile

$$hf_2(x) = h\left[\frac{1}{\exp[\zeta_1(|x+0.5s|-0.5w_1)]+1} + \frac{1}{\exp[\zeta_2(|x-0.5s|-0.5w_2)]+1}\right], \quad (51)$$

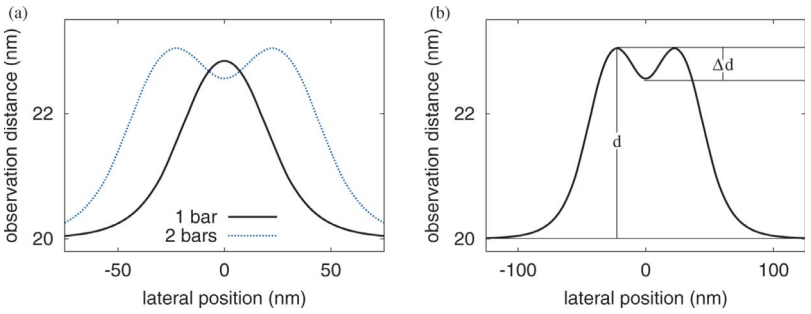

FIG. 6. (Color online) (a) Observation distance above the one-bar gold sample described by Eq. (39) (1 bar), and above the sample with two parallel bars specified by Eq. (51) (2 bars), determined such that the second-order LDOS for $\omega=10^{14}$ s^{-1} constantly keeps that value which is attained for the distance $a_{\mathrm{eff}}=20$ nm far away from the bars. (b) Definition of the quantities d and Δd employed for discussing the resolution of an ideal NSThM.

the length scale in question is their separation s. For our matter-of-principle calculations we again choose $h=5$ nm, together with $w_1=w_2=30$ nm and $\zeta_1=\zeta_2=10^9$ m^{-1}.

In Fig. 6(a) we display second-order results for both the one-bar geometry, and for the two-bar structure with bar separation $s=50$ nm. Here the observation distance a is computed such that the LDOS remains fixed at the value attained for the distance $a_{\mathrm{eff}}=20$ nm above the base plane at positions far away from the bars, always assuming $\omega=10^{14}$ s^{-1}.

In order to discuss the resolution of an idealized NSThM, we make two further assumptions. First, we propose that the sensor is pointlike so that no effects due to the real sensor's extension are considered, implying that we aim at the sensor-independent best possible resolution limit. In reality, the finite sensor size will lead to a lower resolution. Second, we assume that the signal recorded by the device is proportional to the LDOS at the dominant thermal frequency, which actually appears to be quite a good approximation for metallic samples.[12] We then take the ratio $\Delta d/d$, where d is the maximum difference $a-a_{\mathrm{eff}}$ encountered above each of the two identical bars, and Δd denotes the difference between that maximum distance and the minimum distance adopted between the bars, as illustrated in Fig. 6(b). We now stipulate that the two bars can be resolved if $\Delta d/d \geq r$; this number r characterizes the sensitivity of the respective experimental set-up.

In Fig. 7 we plot the ratio $\Delta d/d$ for effective distances $a_{\mathrm{eff}}=20$ nm, 30 nm, and 40 nm, as functions of the bar separation s. If we take $r=0.2$ for the sake of discussion, the resolvable minimum distances are $s_{\mathrm{min}}\approx 50$ nm for $a_{\mathrm{eff}}=20$ nm, $s_{\mathrm{min}}\approx 65$ nm for $a_{\mathrm{eff}}=30$ nm, and $s_{\mathrm{min}}\approx 80$ nm for $a_{\mathrm{eff}}=40$ nm. We emphasize that these figures serve to illustrate the basic principle and should not be taken at face value. The resolution achievable with an actual NSThM device will also depend on the type of surface structure under investigation; a further limit will be imposed by the finite sensor volume. The key message, however, stands out clearly. When scanning an isothermal, nanostructured surface with a near-field scanning thermal microscope, one is able to resolve structures with linear extensions which may fall orders of magnitude below the scale set by the dominant thermal wave length.[12]

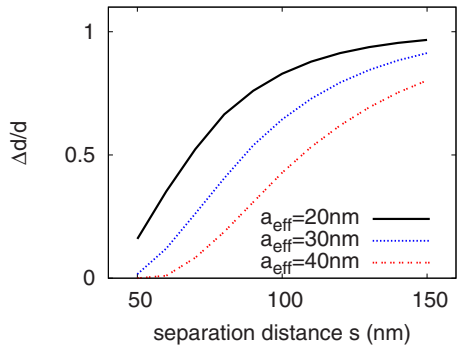

FIG. 7. (Color online) Ratio $\Delta d/d$ for three different values of a_{eff} (20, 30, and 40 nm), as functions of the bar separation s.

IV. CONCLUSIONS

We have demonstrated that a numerical evaluation of Greffet's perturbation series for the scattered electromagnetic field at rough surfaces[26] is routinely feasible up to second order. This allows one to evaluate the local density of states above surfaces with arbitrary profiles, thus lifting the restriction to the limited class of profiles which can be dealt with analytically.

The convergence properties of this series seem to warrant further analysis. While one may reasonably guess that low-order perturbation theory should be sufficient when the profile height h is by far the smallest length scale of the problem, the slow decrease of the successive contributions to the electric LDOS depicted in Fig. 5(a) for the smoothed, but still quite steep metallic model structure sketched in Fig. 1, together with the elementary estimates based on Eq. (42), are warning signs. While our results have been obtained for specific model profiles, it would be quite helpful to have mathematically rigorous and sharp upper bounds on the higher-order contributions for any given surface structure.

We did not discuss possible effects due to the nonlocal dielectric response of the sample, which might come into play at distances of a few nanometers.[42] The question whether such effects would be detectable with a near-field scanning thermal microscope (NSThM) deserves further investigations.

With respect to NSThM surface imaging, we have shown how to estimate the best possible resolution limit, attained for a pointlike sensor. Here we have introduced a mode of operation characterized by constant heat transfer, giving access to isolines of the LDOS. It is now a major task to extend the preliminary studies reported in Ref. 12, considering surfaces with both regular and random nanostructures, and to further explore the concept of near-field thermal imaging.

ACKNOWLEDGMENTS

We wish to thank Achim Kittel, Uli F. Wischnath, David Hellmann, Lars Hoelzel, Ludwig Worbes, and Jürgen Parisi for continuing discussions of their experiments. This work was supported by the Deutsche Forschungsgemeinschaft through Grant No. KI 438/8-1. Computer power was obtained from the GOLEM I cluster of the Universität Oldenburg. S.-A.B. gratefully acknowledges support from the Deutsche Akademie der Naturforscher Leopoldina under Grant No. LPDS 2009-7.

APPENDIX: CALCULATIONAL DETAILS

In this appendix we state the precise forms of the expressions which have been used in Sec. II B. The vector $\boldsymbol{S}^{(1)}$ introduced in Eq. (34), required for computing the first-order electric contribution (33), contains the products of the transmission coefficients $t_{\mathrm{s}}(\boldsymbol{\kappa})=(2k_{z0})(k_{z0}+k_z)^{-1}$ and $t_{\mathrm{p}}(\boldsymbol{\kappa})=(2\sqrt{\epsilon}k_{z0})(\epsilon k_{z0}+k_z)^{-1}$, together with a convenient prefactor:

$$\boldsymbol{S}^{(1)}(\boldsymbol{\kappa},\boldsymbol{\kappa}')=\frac{k_0^2}{\kappa\kappa'}\frac{\epsilon-1}{16\pi^2}\frac{e^{-i(k_{z0}+k'_{z0})z}}{k_{z0}k'_{z0}}\begin{bmatrix} t_{\mathrm{s}}(\boldsymbol{\kappa})t_{\mathrm{s}}(\boldsymbol{\kappa}')\boldsymbol{\kappa}\cdot\boldsymbol{\kappa}' \\ -t_{\mathrm{s}}(\boldsymbol{\kappa})t_{\mathrm{p}}(\boldsymbol{\kappa}')\dfrac{k'_z}{nk_0}(\boldsymbol{\kappa}\times\boldsymbol{\kappa}')_z \\ -t_{\mathrm{p}}(\boldsymbol{\kappa})t_{\mathrm{s}}(\boldsymbol{\kappa}')\dfrac{k_z}{nk_0}(\boldsymbol{\kappa}\times\boldsymbol{\kappa}')_z \\ \dfrac{t_{\mathrm{p}}(\boldsymbol{\kappa})t_{\mathrm{p}}(\boldsymbol{\kappa}')}{n^2k_0^2}[n^2\kappa^2\kappa'^2-k_zk'_z(\boldsymbol{\kappa}\cdot\boldsymbol{\kappa}')] \end{bmatrix}. \tag{A1}$$

The other vector $\boldsymbol{A}_{\mathrm{tr}}^{(\mathrm{E})}$ appearing in Eq. (34) contains the traces of the dyadic products,

$$\boldsymbol{A}_{\mathrm{tr}}^{(\mathrm{E})}(\boldsymbol{\kappa},\boldsymbol{\kappa}')=\frac{1}{\kappa\kappa'}\begin{Bmatrix} \boldsymbol{\kappa}\cdot\boldsymbol{\kappa}' \\ -\dfrac{k'_{z0}}{k_0}(\boldsymbol{\kappa}\times\boldsymbol{\kappa}')_z \\ -\dfrac{k_{z0}}{k_0}(\boldsymbol{\kappa}\times\boldsymbol{\kappa}')_z \\ \dfrac{1}{k_0^2}[\kappa^2\kappa'^2-k_{z0}k'_{z0}(\boldsymbol{\kappa}\cdot\boldsymbol{\kappa}')] \end{Bmatrix}. \tag{A2}$$

For computing the magnetic contribution, this vector has to be replaced by

$$\boldsymbol{A}_{\mathrm{tr}}^{(\mathrm{H})}(\boldsymbol{\kappa},\boldsymbol{\kappa}')=\frac{1}{\kappa\kappa'}\begin{Bmatrix} \dfrac{1}{k_0^2}[\kappa^2\kappa'^2-k_{z0}k'_{z0}(\boldsymbol{\kappa}\cdot\boldsymbol{\kappa}')] \\ \dfrac{k_{z0}}{k_0}(\boldsymbol{\kappa}\times\boldsymbol{\kappa}')_z \\ \dfrac{k'_{z0}}{k_0}(\boldsymbol{\kappa}\times\boldsymbol{\kappa}')_z \\ \boldsymbol{\kappa}\cdot\boldsymbol{\kappa}' \end{Bmatrix}. \tag{A3}$$

The vector $\boldsymbol{S}_1^{(2)}(\boldsymbol{\kappa},\boldsymbol{\kappa}')$ determining the second-order term (35) is given by

$$\boldsymbol{S}_1^{(2)}(\boldsymbol{\kappa},\boldsymbol{\kappa}')=i\frac{k_0^2(\epsilon-1)}{16\pi^2\kappa\kappa'}\frac{e^{-i(k_{z0}+k'_{z0})z}}{k_{z0}k'_{z0}}\begin{bmatrix} t_{\mathrm{s}}(\boldsymbol{\kappa})t_{\mathrm{s}}(\boldsymbol{\kappa}')(k_z+k'_z)(\boldsymbol{\kappa}\cdot\boldsymbol{\kappa}') \\ -t_{\mathrm{s}}(\boldsymbol{\kappa})t_{\mathrm{p}}(\boldsymbol{\kappa}')\dfrac{k'_z}{nk_0}(k_z+k'_z)(\boldsymbol{\kappa}\times\boldsymbol{\kappa}')_z \\ -t_{\mathrm{p}}(\boldsymbol{\kappa})t_{\mathrm{s}}(\boldsymbol{\kappa}')\dfrac{1}{nk_0}(k_zk'_z+n^2k_{z0}^2)(\boldsymbol{\kappa}\times\boldsymbol{\kappa}')_z \\ t_{\mathrm{p}}(\boldsymbol{\kappa})t_{\mathrm{p}}(\boldsymbol{\kappa}')\dfrac{1}{n^2k_0^2}[\kappa^2\kappa'^2(n^2k'_z+k_z)-(\boldsymbol{\kappa}\cdot\boldsymbol{\kappa}')k'_z(k_zk'_z+n^2k_{z0}^2)] \end{bmatrix}, \tag{A4}$$

whereas the vector $\boldsymbol{S}_2^{(2)}(\boldsymbol{\kappa},\boldsymbol{\kappa}',\boldsymbol{\kappa}'')$ entering into the expression (38), and thus into the other second-order contribution (37), takes the form

$$S_2^{(2)}(\boldsymbol{\kappa},\boldsymbol{\kappa}',\boldsymbol{\kappa}'') = -i\frac{k_0^2(\epsilon-1)e^{-i(k_{z0}+k_{z0}'')z}}{8\pi^2\kappa\kappa'^2\kappa''}\frac{k_z'-k_{z0}'}{k_{z0}''k_{z0}}$$
$$\times\left[\begin{array}{l} t_s(\boldsymbol{\kappa})t_s(\boldsymbol{\kappa}'')\left[(\boldsymbol{\kappa}\cdot\boldsymbol{\kappa}')(\boldsymbol{\kappa}'\cdot\boldsymbol{\kappa}'')-\dfrac{k_z'k_{z0}'}{\kappa'^2+k_z'k_{z0}'}(\boldsymbol{\kappa}\times\boldsymbol{\kappa}')_z(\boldsymbol{\kappa}'\times\boldsymbol{\kappa}'')_z\right] \\ -t_s(\boldsymbol{\kappa})t_p(\boldsymbol{\kappa}'')\left[\dfrac{k_z''}{nk_0}(\boldsymbol{\kappa}\cdot\boldsymbol{\kappa}')(\boldsymbol{\kappa}'\times\boldsymbol{\kappa}'')_z+\dfrac{k_z'}{nk_0}\dfrac{\boldsymbol{\kappa}'\boldsymbol{\kappa}''+k_{z0}'k_z''(\boldsymbol{\kappa}'\cdot\boldsymbol{\kappa}'')}{\kappa'^2+k_{z0}'k_z'}(\boldsymbol{\kappa}\times\boldsymbol{\kappa}')_z\right] \\ -t_p(\boldsymbol{\kappa})t_s(\boldsymbol{\kappa}'')\left[\dfrac{k_z}{nk_0}(\boldsymbol{\kappa}\times\boldsymbol{\kappa}')_z(\boldsymbol{\kappa}'\cdot\boldsymbol{\kappa}'')+\dfrac{k_{z0}(\boldsymbol{\kappa}'\times\boldsymbol{\kappa}'')_z}{nk_0}\dfrac{n^2\kappa^2\kappa'^2-k_zk_z'(\boldsymbol{\kappa}\cdot\boldsymbol{\kappa}')}{\kappa'^2+k_{z0}'k_z'}\right] \\ t_p(\boldsymbol{\kappa})t_p(\boldsymbol{\kappa}'')\left[\dfrac{k_z''k_z}{n^2k_0^2}(\boldsymbol{\kappa}\times\boldsymbol{\kappa}')_z(\boldsymbol{\kappa}'\times\boldsymbol{\kappa}'')_z+\dfrac{1}{n^2k_0^2}\dfrac{\kappa'^2\kappa''^2+k_{z0}'k_z''(\boldsymbol{\kappa}'\cdot\boldsymbol{\kappa}'')}{\kappa'^2+k_{z0}'k_z'}[n^2\kappa^2\kappa'^2-k_zk_z'(\boldsymbol{\kappa}\cdot\boldsymbol{\kappa}')]\right] \end{array}\right]. \quad \text{(A5)}$$

*Present address: Laboratoire Charles Fabry, Institut d'Optique, CNRS, Université Paris-Sud, Campus Polytechnique, RD128, 91127 Palaiseau Cedex, France.

[1] S. M. Rytov, Yu. A. Kravtsov, and V. I. Tatarskii, *Principles of Statistical Radiophysics* (Springer, New York, 1989).
[2] K. Joulain, J.-P. Mulet, F. Marquier, R. Carminati, and J.-J. Greffet, Surf. Sci. Rep. **57**, 59 (2005).
[3] A. I. Volokitin and B. N. J. Persson, Rev. Mod. Phys. **79**, 1291 (2007).
[4] L. Hu, A. Narayanaswamy, X. Chen, and G. Chen, Appl. Phys. Lett. **92**, 133106 (2008).
[5] A. Narayanaswamy, S. Shen, and G. Chen, Phys. Rev. B **78**, 115303 (2008).
[6] S. Shen, A. Narayanaswamy, and G. Chen, Nano Lett. **9**, 2909 (2009).
[7] E. Rousseau, A. Siria, G. Jourdan, S. Volz, F. Comin, J. Chevrier, and J.-J. Greffet, Nat. Photonics **3**, 514 (2009).
[8] D. Polder and M. van Hove, Phys. Rev. B **4**, 3303 (1971).
[9] W. Müller-Hirsch, A. Kraft, M. T. Hirsch, J. Parisi, and A. Kittel, J. Vac. Sci. Technol. A **17**, 1205 (1999).
[10] A. Kittel, W. Müller-Hirsch, J. Parisi, S.-A. Biehs, D. Reddig, and M. Holthaus, Phys. Rev. Lett. **95**, 224301 (2005).
[11] U. F. Wischnath, J. Welker, M. Munzel, and A. Kittel, Rev. Sci. Instrum. **79**, 073708 (2008).
[12] A. Kittel, U. F. Wischnath, J. Welker, O. Huth, F. Rüting, and S.-A. Biehs, Appl. Phys. Lett. **93**, 193109 (2008).
[13] Y. De Wilde, F. Formanek, R. Carminati, B. Gralak, P.-A. Lemoine, K. Joulain, J.-P. Mulet, Y. Chen, and J.-J. Greffet, Nature (London) **444**, 740 (2006).
[14] R. S. DiMatteo, P. Greiff, S. L. Finberg, K. A. Young-Waithe, H. K. H. Choy, M. M. Masaki, and C. G. Fonstad, Appl. Phys. Lett. **79**, 1894 (2001).
[15] A. Narayanaswamy and G. Chen, Appl. Phys. Lett. **82**, 3544 (2003).
[16] M. Laroche, R. Carminati, and J.-J. Greffet, J. Appl. Phys. **100**, 063704 (2006).
[17] M. Francoeur, M. P. Mengüç, and R. Vaillon, Appl. Phys. Lett. **93**, 043109 (2008).
[18] S. Basu, Z. M. Zhang, and C. J. Fu, Int. J. Energy Res. **33**, 1203 (2009).
[19] K. Joulain, R. Carminati, J.-P. Mulet, and J.-J. Greffet, Phys. Rev. B **68**, 245405 (2003).
[20] I. A. Dorofeyev, J. Phys. D: Appl. Phys. **31**, 600 (1998).
[21] J. B. Pendry, J. Phys.: Condens. Matter **11**, 6621 (1999).
[22] J.-P. Mulet, K. Joulain, R. Carminati, and J.-J. Greffet, Appl. Phys. Lett. **78**, 2931 (2001).
[23] G. V. Dedkov and A. A. Kyasov, Tech. Phys. Lett. **33**, 305 (2007).
[24] I. Dorofeyev, Phys. Lett. A **372**, 1341 (2008).
[25] P.-O. Chapuis, M. Laroche, S. Volz, and J.-J. Greffet, Phys. Rev. B **77**, 125402 (2008).
[26] J.-J. Greffet, Phys. Rev. B **37**, 6436 (1988).
[27] S.-A. Biehs, O. Huth, and F. Rüting, Phys. Rev. B **78**, 085414 (2008).
[28] S.-A. Biehs and J.-J. Greffet, Phys. Rev. B **81**, 245414 (2010).
[29] G. A. Farias and A. A. Maradudin, Phys. Rev. B **28**, 5675 (1983).
[30] C. Henkel and V. Sandoghdar, Opt. Commun. **158**, 250 (1998).
[31] A. Lambrecht, P. A. Maia Neto, and S. Reynaud, New J. Phys. **8**, 243 (2006).
[32] P. M. van den Berg and J. T. Fokkema, J. Opt. Soc. Am. **69**, 27 (1979).
[33] J. P. Hugonin, R. Petit, and M. Cadilhac, J. Opt. Soc. Am. **71**, 593 (1981).
[34] J. B. Keller, J. Opt. Soc. Am. A **17**, 456 (2000).
[35] A. G. Ramm, J. Phys. A **35**, L357 (2002).
[36] L. B. Felsen and N. Marcuvitz, *Radiation and Scattering of Waves* (IEEE, New York, 1994).
[37] T. Hahn, Comput. Phys. Commun. **176**, 712 (2007).
[38] M. Frigo and S. G. Johnson, Proc. IEEE **93**, 216 (2005).
[39] N. W. Ashcroft and N. D. Mermin, *Solid State Physics* (Harcourt, Fort Worth, 1976).
[40] C. F. Klingshirn, *Semiconductor Optics* (Springer, New York, 2005).
[41] S. Adachi, *Handbook on Physical Properties of Semiconductors* (Kluwer Academic, Boston, 2004), Vol. 2.
[42] C. Henkel and K. Joulain, Appl. Phys. B: Lasers Opt. **84**, 61 (2006).